GPS displacement dataset for study of elastic surface mass variations

Athina Peidou[1], Donald Argus[1], Felix Landerer[1], David Wiese[1] and Matthias Ellmer[1]

Jet Propulsion Laboratory, California Institute of Technology, Pasadena, CA, USA, 2023

Correspondence to: Athina Peidou (athina.peidou@jpl.nasa.gov)

Abstract

Quantification of uncertainty in surface mass change signals derived from GPS measurements poses challenges, especially when dealing with large datasets with continental or global coverage. We present a new GPS station displacement dataset that reflect surface mass load signals and their uncertainties. We assess the structure and quantify the uncertainty of vertical land displacement derived from 3045 GPS stations distributed across the continental US. Monthly means of daily positions are available for 15 years. We list the required corrections to isolate surface mass signals in GPS estimates and screen the data using GRACE(-FO) as external validation. Evaluation of GPS timeseries is a critical step, which identifies a) corrections that were missed; b) sites that contain non-elastic signals (e.g., close to aquifers); and c) sites affected by background modelling errors (e.g., errors in the glacial isostatic model). Finally, we quantify uncertainty of GPS vertical displacement estimates through stochastic modeling and quantification of spatially correlated errors. Our aim is to assign weights to GPS estimates of vertical displacements, which will be used in a joint solution with GRACE(-FO). We prescribe white, colored and spatially correlated noise. To quantify spatially correlated noise, we build on the common mode imaging approach adding a geophysical constraint (i.e., surface hydrology) to derive an error estimate for the surface mass signal. We study the uncertainty of the GPS displacement timeseries and find an average noise level between 2-3 mm when white noise, flicker noise, and RMS of residuals about a seasonality and trend fit are used to describe uncertainty. Prescribing random walk noise increases the error level such that half of the stations have noise > 4 mm, which is systematic with the noise level derived through modeling of spatial correlated noise. The new dataset is suitable for use in a future joint solution with GRACE(-FO)-like observations.

Keywords: GPS uncertainty | elastic displacement | GRACE-FO | surface mass change

1. Introduction

For more than two decades, the Gravity Recovery and Climate Experiment (GRACE) space gravity mission and its nearly identical successor mission, GRACE-Follow on (GRACE-FO), have provided mass change estimates through tracking the time-variable part of the Earth's gravity field (Landerer et al., 2020). Mass change products are typically given on a monthly basis and have been used to study a variety

40   of critical climate-related factors (Tapley et al., 2019), such as sea level rise (Frederikse et al., 2020); ice
41   mass change (Velicogna et al., 2020); prolonged drought periods (Thomas et al., 2014) and regional flood
42   potentials (Reager et al., 2014). The measurement geometry of GRACE(-FO) limits the study of
43   geophysical processes to spatial scales of ~300 km and larger, for monthly timespans. Recent community
44   reports (Pail et al., 2015, Wiese et al., 2022) have highlighted the utility and need of mass change
45   observations at improved spatial resolutions to address a number of science and applications objectives.
46   Examples include closure of the terrestrial water budget for small to medium sized river basins, and
47   separation of surface mass balance from ice dynamic processes at the scale of individual outlet glacier
48   systems.
49   The spatial resolution of gravity maps derived from satellite measurements is limited by sampling at
50   altitude. Fusion with external geodetic data sources, however, can improve spatial resolution over what
51   can be achieved only with satellite gravimetry. GPS position timeseries have been used widely to study
52   the elastic response of Earth's surface to mass loading (e.g., Argus et al., 2017; Fu and Freymueller,
53   2012) and can provide information at short wavelengths (~100km) (Argus et al., 2021). Solid Earth
54   responds elastically to changes in the surface load of water, snow, ice, and atmosphere. When the Earth's
55   surface is loaded with mass (e.g., snow and water) it subsides; and when mass loads are removed the
56   surface rises. Thus, the Earth's response follows the water cycles such that: precipitation and snow
57   accumulation cause subsidence of the surface and snow melt, evaporation and water run off allow the
58   Earth's surface to bounce back (uplift). Focus is typically placed on the radial direction (vertical), due to
59   the rapid decrease of vertical displacement with the distance from a surface load (Argus et al., 2017),
60   which leads to high fidelity estimates in the space domain. Note that across certain geological formations
61   such as aquifers, subduction zones and regions with volcanic activity surface loading is mixed with other
62   solid Earth/geophysical processes making it difficult to isolate the elastic component. Therefore, GPS
63   sites located at the vicinity of such formations are omitted.
64   GPS displacements between two epochs have many different signals embedded in them; i.e., those related
65   to non-tidal atmospheric and oceanic loading, solid Earth phenomena such as tectonics, glacial isostatic
66   adjustment, and others related to surface mass changes. With the proper treatment (see Section 2) GPS
67   stations can capture local surface mass changes. We are interested in isolating the signals that reflect the
68   Earth's elastic response to mass variations, thus we apply a set of corrections to GPS vertical
69   displacement estimates, and then we screen the data for outliers or potential errors. The data screening
70   process checks for consistency between GPS and GRACE(-FO) vertical displacement estimates (similar
71   analysis has been performed by Yin et al., 2020; Blewitt et al., 2001; van Dam et al., 2001; Becker and
72   Bevis, 2004; Davis, 2004; Tregoning et al., 2009; Tsai, 2011 and Chew et al., 2014) and identifies outliers
73   that statistical tests fail to pick up (He et al., 2018).
74   The last step is to estimate uncertainty in the screened dataset. Since our purpose is to isolate surface mass
75   load signals, we define *error* as any vertical displacement signal that does not reflect an elastic surface
76   mass load. The reported uncertainty reflects the sum of all error sources to the measurement and is the
77   final product of this study. Error correlation (temporal and spatial) and the deficiency of stochastic noise
78   models to describe the error realistically are the main challenges in this uncertainty quantification task.
79   Error sources include errors driven by satellite antenna phase centre offsets (Haines et al., 2004;
80   Santamaria-Gomez et al., 2012); atmospheric pressure models (Kumar et al., 2020); non-tidal ocean
81   loading (Jiang et al., 2013); satellite orbits (Ray et al., 2008; Amiri-Simkooei ,2013); earth orientation
82   parameters (Rodriguez-Solano et al., 2014); and tectonic trends and post-seismic relaxation after
83   earthquake activity (Ji and Herring, 2013; Crowell et al., 2016).

84   The GPS position timeseries have common mode displacements [Tian and Shen 2016], including both a
85   common mode error strongly varying each day and a common mode signal associated with seasonal water
86   fluctuations. Wdowinski et al. (1997) first defined common mode error to be a series of rigid-body
87   translations that reflect an error in the position of all geodetic sites in an area relative to an absolute
88   reference frame; by removing the mean position (or stack) of all sites in an area, scientists recover more
89   accurate estimates of relative position contained in the data. Dong et al. (2006) and Serpelloni et al.
90   (2013) defined common mode error in a more sophisticated manner using principal or independent
91   component analysis such that they remove spatially correlated, temporally incoherent error. Independent
92   is different than principal component analysis in that it finds the maximum independence of the
93   components instead of minimum correlation (Milliner et al., 2019; Liu et al., 2015). Common mode
94   displacements includes both error (such as that associated with error in satellite orbits) and signal (such as
95   the seasonal oscillation of elastic vertical displacement in elastic response to seasonal fluctuations in mass
96   between the hemispheres) (Sun et al. 2016).
97   Considering the increased number of GPS stations and the limitations posed by the existing
98   methodologies, Kreemer and Blewitt (2021) used a robust methodology to estimate the common spatial
99   components of GPS residuals (i.e., the remaining signals of a timeseries after subtraction of a trajectory
100 model). A trajectory model is a model consisting of an offset, a rate, and a sinusoid with a period of 1
101 year (Bevis and Brown, 2014). The so-called common mode component (CMC) imaging technique was
102 originally introduced by Tian and Shen (2016) and quantifies the spatial correlation of the residuals
103 (position or vertical displacement timeseries anomaly with respect to a trajectory model) of unequal-
104 length timeseries using information from neighbor stations. It is important to note that CMC reflects both
105 spatially correlated noise and spatially correlated signals, including elastic displacements, that a trajectory
106 model fails to describe.
107 Spectral analysis of the residuals (with respect to a trajectory model, see Eq.2) is an alternative way to
108 estimate the noise level of vertical displacement series for each GPS station. The spectrum of the
109 residuals can be approximated by white or colored noise (flicker, random walk, power law approximation,
110 generalized gauss markov etc.), or by a combination of white and colored noise (Williams et al., 2004;
111 Bos et al., 2008; Klos et al., 2014). A summary of the different noise models and their power distribution
112 can be found in He et al. (2018). Several standard GPS timeseries analysis packages are available to
113 perform such an analysis, e.g., the Create and Analyze Timeseries (CATS) (Williams, 2008) and Hector
114 (Bos et al. 2013). Various studies in the past suggested that the residuals are better described by a
115 combination of white and flicker noise (see e.g., Klos et al., 2014; Argus et al., 2017), with the latter
116 contributing the most (Argus and Peltier, 2010). Recently, Argus et al. (2022), showed that the longer the
117 timeseries the more the spectrum of GPS residuals converges with the noise model of random walk.
118
119 Here, we outline a comprehensive framework for processing large datasets (continental and/or global) of
120 GPS timeseries, to derive estimates that only reflect surface mass signals, for use in a joint inversion with
121 GRACE(-FO) measurements. Originally, we layout the corrections required to capture local surface mass
122 changes (Section 2.1). Our interest is to make the process as automated as possible, thus we set a number
123 of evaluation metrics to detect outliers among all candidate (for the joint inversion) sites. Stations flagged
124 as outliers are further evaluated for extra corrections (e.g., offsets; poor site maintenance etc.). Finally, we
125 assign weights to each GPS vertical displacement record. We test the most popular methodologies to
126 quantify the error, considering time-correlation, spatial-correlation and/or white noise (Section 3). Note
127 that for spatially correlated noise the commonly used PCA/ICA is not as applicable to our use case,

128 because our dataset extends over very large spatial areas (continental). CMC imaging (Kreemer and
129 Blewitt; 2021) fits our needs better. We build on the existing CMC algorithm to remove hydrology
130 signals from the error estimate by deriving surface loading signals from a hydrology model and removing
131 them from the GPS vertical displacements (see Section 3 for more details). The final product is a new
132 dataset with GPS vertical displacement estimates that reflect elastic mass variations and their
133 uncertainties.
134
2. GPS data processing and screening

136
2.1 Isolating surface mass loading fingerprint from GPS vertical displacements
138 We analyze positions of 3054 GPS sites as a function of time from 2006 to 2021 estimated by scientists at
139 the Nevada Geodetic Laboratory (NGL) (Blewitt et al. 2018). Technologists at Jet Propulsion Laboratory
140 (JPL) first estimate satellite orbits, satellite clocks, and positions for a core set of roughly 50 sites on
141 Earth's surface (Bertiger et al. 2020). NGL uses JPL's clock and orbit products and performs point
142 positioning to a total of about 18,500 GPS sites distributed across the world. Following the International
143 Earth Rotation Standards (IERS) (Petit and Luzum, 2012) NGL's positions are corrected for solid Earth,
144 ocean, and pole tides. NGL's positions in International Terrestrial Reference Frame 2014 (ITRF2014)
145 (Altamimi et al. 2016) are more accurate than NGL's previous estimates of positions in ITRF2008. NGL
146 estimates GPS wet tropospheric delays each day using the ECMWF weather model (Simmons et al. 2007)
147 and the VMF1 tropospheric mapping function (Boehm et al. 2006). We input the NGL position
148 timeseries, derive the displacement relative to a reference epoch and then follow Argus et al. (2010, 2017,
149 2021) to isolate the part of GPS displacements reflecting solid Earth's elastic response:

151 a. Construct timeseries of elastic displacement uninterrupted by offsets due to antenna substitutions or
152 earthquakes that pass through a specific reference time (such as Jan 1, 2014) by eliminating data before
153 and /or after an offset.

155 b. Identify and omit GPS sites recording primarily i. poreoleastic response to change in groundwater, ii.
156 strong volcanic fluctuations, and iii. postseimic transients following Argus et al. (2014, 2017, 2022). In
157 the west U.S., GPS sites responding to groundwater change have maximum height around April when
158 water is maximum, subside in the long term faster than 1.8 mm/yr, exhibit strong transients, and/or are
159 located in known aquifers (Argus et al. 2014). Volcanic activity is readily identified by Interferometric
160 Synthetic Aperture Radar (InSAR) and GPS observations of strong transients and anomalous sustained
161 uplift or subsidence (Argus et al. 2014, Hammond et al. 2016).

163 c. Remove non-tidal atmospheric (NTAL) and non-tidal oceanic (NTOL) mass loading by interpolating
164 global grids of elastic displacements calculated by the German Center for Geoscience (GFZ) (Dill
165 Dobslaw, 2013) following the method of Martens et al. (2020).

167 d. Remove glacial isostatic adjustment as predicted by model ICE-6G_D (VM5a) (Peltier et al. 2015,
168 2018; Argus et al. 2014).

170 e. Remove interseismic strain accumulation associated with locking of the Cascadia subduction zone
171 using an upgrade of the model of Wang et al. (2018). The model is superposition of 2/3 of the elastic and

172 1/3 of the viscoelastic model of Wang et al. (2018). We communicated with Li Wang and his team at
173 National Resources Canada, that the Wang et al. (2018) model does not fit the available GPS data; they
174 have produced an interim model using our input that more nearly fits the GPS data.
175
176 f. Average the daily estimates of GPS vertical displacements into monthly means centered at the center of
177 each month from January 2006 to June 2021.
178
179 To compare GPS with GRACE(-FO) vertical displacement estimates we reference the series to the epoch
180 with the most GPS site records, which is September 2012. This process results in an 11% loss of stations
181 (i.e., no available measurement on 09/2012). Similar to Yin et al. (2020), detrended monthly estimates of
182 each station that are larger than 3σ relative to the mean of the timeseries are considered outliers and
183 removed from the dataset. Statistical outliers comprise ~0.5% of the records.
184 2705 (or 88.8%) of GPS stations remain after the choice of reference epoch, the 3σ test and the removal
185 of sites with non-elastic loading response. The distribution of sites is denser along the East and West
186 coasts, and fairly sparse in the central-north US (Fig.1). Series of two arbitrary stations (HIVI and NJWT)
187 located at the West and East coast respectively, are shown in Fig. 1. The response of the Earth on the
188 extensive drought period in California between 2011.5-2015.5 is captured in the uplift trend mapped by
189 HIVI station (Fig.1, top right panel; dashed blue line).
190
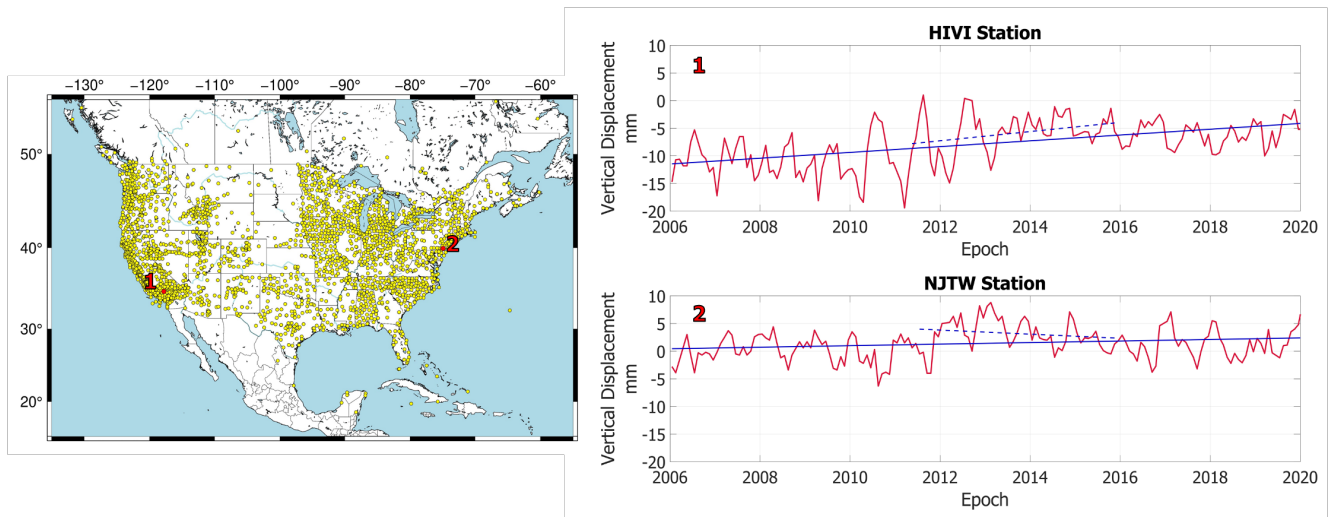
191
192 Figure 1: Left panel) Map of study area. GPS stations are shown in yellow; Right panel) Vertical
193 displacement timeseries of two random stations (red line). Solid blue line denotes the overall trend of the
194 timeseries and dashed blue line the trend between (2011.5-2015.5). Note the significant uplift of the HIVI
195 station located in southern California.
196
197 2.2 External validation datasets - Time-variable gravity field
198
199 We compare GPS observations of vertical displacement against GRACE(-FO) estimates of solid Earth's
200 elastic vertical displacement from terrestrial water, snow, and ice.
201 To compare to GRACE(-FO), we analyze JPL's three-degree mascon solution (Release 6, Watkins et al.
202 2015, Wiese et al. 2016). The effect of glacial isostatic adjustment is removed from GRACE(-FO)
203 products using ICE-6G_D model estimates (Peltier et al., 2017). The geocentre motion (degree 1)

204 coefficient is using the technique of Sun et al. (2016) (Technical Note 13). Values of C20 (Earth's
205 oblateness) and C30 (for months after Aug 2016) are substituted with SLR data (Loomis et al., 2019). We
206 calculate solid Earth's elastic response by using the loading Love number of the Preliminary Reference
207 Earth Model (Wang et al.; 2012).
208 Estimates of GPS positions in ITRF2014 (Altamimi et al. 2016) are relative to center of mass (CM) in the
209 long term but relative to center of figure (CF) in the seasons (because ITRF2014 does not allow there to
210 be seasonal oscillations of CM). We therefore remove the long-term rate of CM relative to CF to
211 transform the GRACE estimates in the long term from CF to CM (but do not remove seasonal oscillations
212 of CM relative to CF so as to preserve the ITRF seasonal frame relative to CF). The annual signal of the
213 geocenter (as realized by ITRF 2014) projected on the up component in north America on average
214 explains 3% of the GPS vertical displacement signal and can explain up to 20% for certain sites.
215 GRACE(-FO) vertical displacement monthly estimates are derived as follows (e.g., Davis et al., 2004):
216

$$U(\phi, \lambda) = a \sum_{l,m} \left(\frac{h_l^E}{1 + k_l^E} \right) P_{lm}(sin\lambda) \times [C_{lm}cosm\phi + S_{lm}sinm\phi] \tag{1}$$

218 Where, U is the estimate of vertical displacement, a denotes the Earth's radius, ϕ, λ denote the latitude
219 and longitude, respectively; P_{lm} are the associated Legendre polynomials, k_l^E and h_l^E are the elastic
220 gravity and vertical load Love numbers (Wang et al., 2012), respectively, and C and S are the spherical
221 harmonic coefficients derived from GRACE(-FO) monthly solutions with respect to degree l and order
222 m. JPL releases gridded mascon fields, to derive spherical harmonics (C and S in Eq. 1). We transform
223 fields of equivalent water height to normalized harmonic coefficients using the inverse of Eq. 9 in Wahr
224 et al. (1998). Like GPS, we subtract the GRACE(-FO) vertical displacement field of September 2012
225 from each monthly field to establish a common reference basis. GRACE(-FO) fields are estimated at a
226 0.5-degree spatial resolution (ϕ, λ in Eq.1). Thus, we extract GRACE(-FO) estimates at the station level
227 by interpolating bilinearly the vertical displacement from the nearest 0.5-degree grid point neighbors to
228 the station's location.
229
230 2.3 Screening metrics
231
232 GPS vertical displacement estimates are evaluated against the ones derived from GRACE(-FO), to assist
233 in identifying outliers or further corrections that may be needed. We employ a number of different metrics
234 to evaluate the agreement between the two datasets, and to determine whether to include it in the joint
235 solution or not. Similar to Yin et al. (2020) we quantify correlation and variance reduction between GPS
236 and GRACE(-FO) vertical displacements. The structure of surface mass periodic signals (e.g., annual
237 cycles, trends) as picked up by the two measurement techniques, also entails critical information
238 regarding mismodelled offsets, and is evaluated as well.
239 This process flags sites that need correction and corroborates joint inversion's hypothesis (Argus et al.,
240 2021), that a basic level of agreement is needed for the GPS data to be used to infer surface mass change.
241
242
243
244

245 *Correlation*
246
247 First, we specify the level of agreement between the datasets by estimating the Pearson correlation
248 coefficient between GPS and GRACE(-FO) timeseries. On average correlation is 62%, but stations
249 located on the West coast exhibit an agreement higher than 80%, which in most cases is driven by the
250 larger annual signal amplitude there. A more detailed look into the correlation metric is performed to
251 evaluate the agreement of GPS/GRACE(-FO) in retrieving the seasonal cycle amplitude in different
252 watersheds. We fit and remove a trajectory model $y(t)$:
253

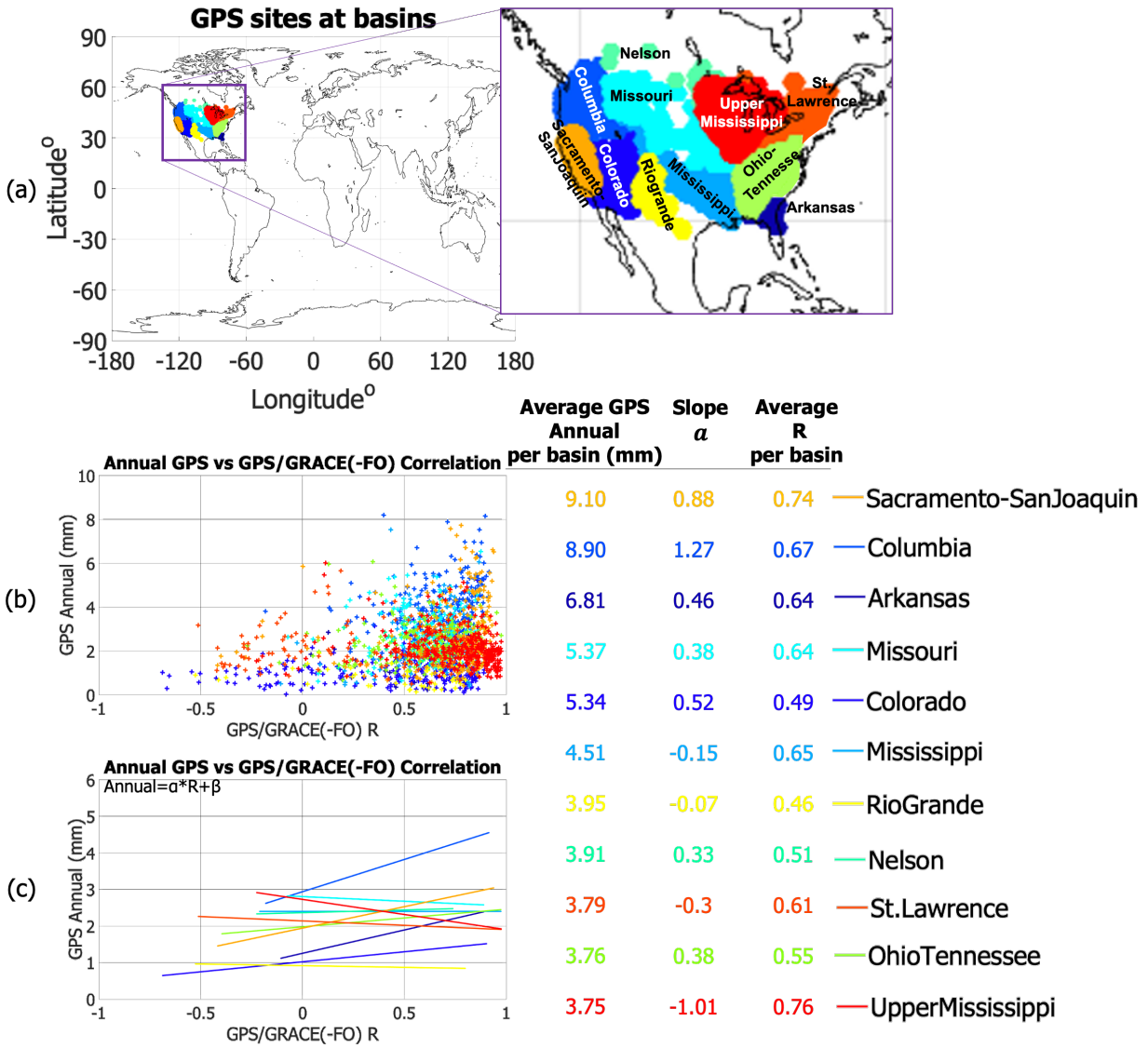$$y(t) = a + bt + A\sin(2\pi t) + B\cos(2\pi t), \tag{2}$$

254
255 with a being the intercept; b being the trend and A and B being the amplitudes of the sine and cosine
256 components of a periodic function. In a future release of the dataset, we will evaluate the presence of
257 draconitic periods in the time-series and add them in the trajectory model if justified. With the timespan
258 of the current timeseries being up to 15 years, we cannot resolve for the draconitics (i.e., the first
259 draconitic period (351.6 days) and the annual cycle (365.25 days) are very close and require a long time-
260 series to be deciphered). For a more thorough discussion we refer the interested reader to Amiri-Simkooei
261 et al. (2017) and Klos et al. (2023).
262
263 We classify stations in watersheds and plot the GPS-GRACE(-FO) correlation coefficient (R) of each
264 station in different watershed against the amplitude of annual signals (Fig. 2b). To quantify the
265 relationship between magnitude of the annual cycle and correlation between the two datasets we fit a
266 linear function between the magnitude of the annual signals and the GPS-GRACE(-FO) vertical
267 displacement correlations for each watershed, separately. A steep slope ($\boldsymbol{a}$) of the fit ($\boldsymbol{a}$>0.5) indicates an
268 agreement between the two datasets, which depends on the magnitude of the annual cycle. This
269 relationship breaks when stations of a basin exhibit smaller annual cycles. We discuss an interesting case
270 in Supplements, where stations located in the Great Lakes region (part of the St. Lawrence watershed)
271 demonstrate a negative trend $\boldsymbol{a} = -1.26$. The disagreement is even more pronounced while assessing the
272 second metric (i.e., trends). Both metrics, when taken together, helped us identify the source problem (i.e.,
273 unlogged offset that affected nearly 25% of the stations located in the St. Lawrence watershed) and take
274 corrective actions (see Supplements for more details). Note that for Figs. 2 and 3 the corrected data were
275 used.
276
277

GPS sites at basins

Annual GPS vs GPS/GRACE(-FO) Correlation

Annual GPS vs GPS/GRACE(-FO) Correlation
Annual=α*R+β

Average GPS Annual per basin (mm)	Slope a	Average R per basin	
9.10	0.88	0.74	—Sacramento-SanJoaquin
8.90	1.27	0.67	—Columbia
6.81	0.46	0.64	—Arkansas
5.37	0.38	0.64	—Missouri
5.34	0.52	0.49	—Colorado
4.51	-0.15	0.65	—Mississippi
3.95	-0.07	0.46	—RioGrande
3.91	0.33	0.51	—Nelson
3.79	-0.3	0.61	—St.Lawrence
3.76	0.38	0.55	—OhioTennessee
3.75	-1.01	0.76	—UpperMississippi

Figure 2: a) GPS sites clusters at watersheds in the US. Each watershed has a different color; b) Magnitude of annual GPS vertical displacement cycles derived with respect to GPS-GRACE(-FO) correlation; c) Linear fit between magnitude of the annual GPS vertical displacement cycles and GPS-GRACE(-FO) correlation.

Trends

In order to study the agreement between GPS/GRACE(-FO) in more detail, we split the timeseries of each station into non-overlapping intervals of 36 months, and fit Eq.2 for each station during each time-window. Different time-lengths of the GPS series may lead to misinterpretation of the geophysical content. For example, a station that has records only for the first 13 months out of the total of 36 months window may reflect different fit constituents compared to a neighbor station with full records, if the actual behavior of Earth's response changes during the 36-months window. Although in our dataset this

8

case is rare, we proceed with deriving the rate (slope) and the annual cycles only for stations that have records for at least 28 out of the 36 months. We did not interpolate the series during the GRACE(-FO) gap; thus, the last time-window reflects trends estimated using only GRACE-FO and GPS timeseries between June 2018-2021. As expected, GPS rates feature higher spatial variability than GRACE(-FO). However, both techniques capture large-scale quasi-periodic variations every 3 years (Fig. 3), an agreement that is noteworthy. The effect of this metric to detect outliers is pronounced when the two techniques show flipped trends.

Regions with pronounced trend disagreement:
- St. Lawrence watershed (stations located in the Great Lakes region at the State of Michigan): The trend during 2015-2018 was flipped between GPS and GRACE(-FO) in 62 stations (St. Lawrence watershed has a total of 243 stations available between 2015-2018). We discovered a missed offset in the series occurring in April 2016, and corrected for it, which led to an improved agreement in the trend (see Supplements).
- Cascadia region (northwest coast): The disagreement is evident in maps spanning 2009-2012, 2015-2018 and 2018-2021.5. GPS sites record a large surface uplift, which over the course of 15 years sums to 60 mm in sites located in Vancouver Island. GRACE(-FO) does not capture any such behavior. We attribute this disagreement partly on 1) glacial isostatic adjustment modeling error which manifests oppositely on two techniques. ICE6G_D predicts too much subsidence, thus when we correct GPS, we find too much uplift and when we correct GRACE(-FO) we find too much water gain which predicts too much subsidence; and partly on 2) the interseismic strain accumulation correction applied in the GPS dataset over this area (Argus et al., 2021). The sites have been flagged and are not going to be used in the joint inversion.
- San Andreas Fault (Southern California): Sites located in a vicinity of the Parkfield segment of the fault (Carrizon plain), exhibit consistent disagreement in the trend. More investigation is required to understand the mechanism that the fault presents on GPS/GRACE(-FO) vertical displacement estimates. The disagreement is also seen in Argus et al. (2022, Fig. S12). The sites have been flagged and are not going to be used in the joint inversion.
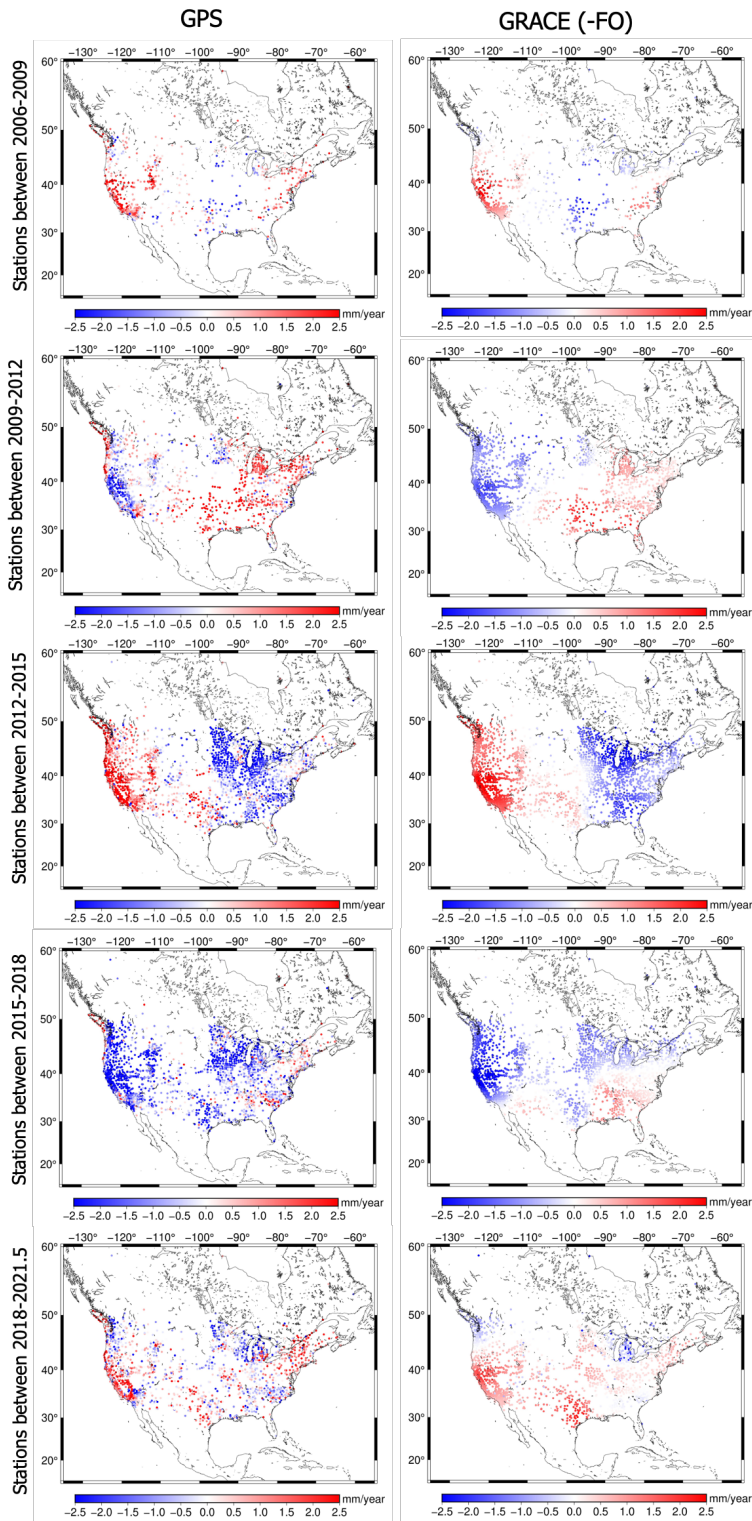
322
323   Figure 3: Rates of vertical displacements derived by GPS and GRACE. The rates are calculated every 36-
324   months (3 years) between 2006-2021.

325
326

327   *Variance Reduction*
328
329   Similarity in both amplitude and phase between two quantities is quantified via the variance attenuation
330   factor (Gaspar and Wunsch, 1989; Fukumori et al., 2015):
331

$$var_{red} = \left(1 - \frac{var(GPS - GRACE(-FO))}{var(GPS)}\right) \times 100 \qquad (3)$$

332
333   The higher the agreement in phase and amplitude between GPS and GRACE(-FO)*,* the closer the metric
334   gets to 100%. var_{red} may also be negative when the differences in amplitude and/or phase are large.
335   Overall, GPS and GRACE(-FO) are consistent when var_{red} exceeds 50%. The areas of main
336   disagreement are near coasts, especially along the Atlantic Ocean. This inconsistency can be partly
337   explained by modeling errors of the non-tidal oceanic and atmospheric loading model (e.g., Klos et al.,
338   2021; van Dam et al., 2007). Additionally, agreement is poor for sites located in the vicinity of the
339   Parkfield segment (specific regions across the fault perform poorly), which is consistent with the
340   disagreement shown in Fig. 3.
341
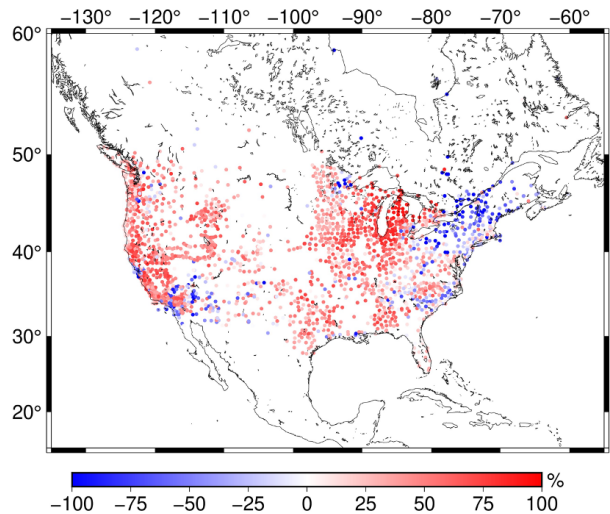
343   Figure 4: Variance reduction between GPS and GRACE(-FO) vertical displacements

344
345   We also compared the annual amplitudes of GPS and GRACE(-FO) vertical displacements (cosine and
346   sine components in Eq. 2). This analysis was not informative for the presence of outliers or errors in the
347   current data sample studied.
348
349   Overall, the screening process not only assisted in outlier detection, but it also allowed for a deeper look
350   into the structure of vertical displacement periodic signals. We identified the need for antenna offset
351   corrections (in sites located in the Great Lakes region); removed sites affected by glacial isostatic
352   adjustment and interseismic modeling errors; and sites located at the Parkfield segment of San Andreas
353   Fault.
354

11

3. Uncertainty Quantification

With the updated dataset we are now ready to proceed with the uncertainty quantification of the GPS vertical displacement timeseries. We apply different error characterization schemes consisting of a root sum square of a random error, white noise error, power law noise error (flicker noise and random walk) and spatially coherent error.

3.1 Methods

Root Mean Square Error

Residuals r of a series with respect to a trajectory model (Eq. 2) are often used as a first approximation of noise in vertical displacement series (e.g., Bos et al., 2013; Michel et al., 2021). Practically, r shows how well a trajectory model can describe the original timeseries. Therefore, the root mean square (rms) of r can give a first approximation of the noise floor of each station.

Spectral Analysis, White, Flicker and Random Walk Noise

Power distribution of residuals and its agreement with noise models, is another popular way to quantify uncertainty of GPS timeseries (e.g., Klos et al., 2019; Argus et al., 2022). Typically, GPS series are evaluated for white, flicker and random walk noise, or combination of them. Hector software (Bos et al., 2013) is used to estimate full noise covariance information by means of a maximum likelihood estimator. The covariance matrix C from a combination of white and power law (i.e., flicker and random walk) noise is given as:

$$C = a \times I + b \times J \qquad \text{Eq. 4}$$

Where a is the amplitude of white noise, I is the identity matrix of size N (number of samples/epochs in the series), b is the amplitude and J the covariance matrix of power law noise. J matrix is a full covariance matrix that describes the time-correlated error (as the data record length increases, the displacement uncertainty changes (Bos et al., 2008 Eqs. 8-11)). The optimal selection of the noise models is done via two optimality criteria, namely the Akaike Information Criterion (Akaike, 1974) and the Bayesian Criterion (Schwarz, 1978).

In this study, we consider three cases:
a)   White Noise (WN)
b)   Combination of WN and Flicker Noise (WN+FN)
c)   Combination of WN, FN and Random Walk Noise (WN+FN+RW)
We take the root-sum-squares of the noise magnitudes as our noise floor. For example, for the case of WN+FN noise, noise is derived as $\sigma = \pm\sqrt{\sigma_{WN}^2 + \sigma_{FN}^2}$. Our data are sampled on a monthly basis, thus

394 σ_{FN} needs to be scaled appropriately, i.e., $\sigma_{FN} = \sigma_{PL}(\frac{1}{12})^{-\frac{k}{4}}$, where, σ_{PL} is the uncertainty of power-law
395 (PL) and k the spectral index, outputted from Hector (more information on power-law noise estimation
396 can be found in Bos et al., 2008, and Williams, 2003).
397
398 *Common Mode Noise*
399
400 The Common Mode Component (CMC) is derived following the processing scheme suggested by
401 Kreemer and Blewitt (2021), which can be summarized as:
402
403 1) Input GPS displacement timeseries (referenced to Sep 2012) for j stations (l_j)
404 2) Derive each station's residuals by removing the trajectory part of the series ($l_j(t) - y_j(t)$)
405 3) Quantify the correlation coefficient r_{MAD} using robust statistics. r_{MAD} is defined as:

$$r_{MAD} = \frac{MAD^2(u) - MAD^2(v)}{MAD^2(u) + MAD^2(v)}$$

Eq. 5

406

407 The median absolute deviation (MAD) is the absolute deviation around the median. For example, for a
408 residual series res(t) $MAD = |res(t) - median(res(t))$. u and v are derived as:

$$u = \frac{p - median(p)}{\sqrt{2}MAD(p)} + \frac{q - median(q)}{\sqrt{2}MAD(q)}$$

Eq. 6

$$v = \frac{p - median(p)}{\sqrt{2}MAD(p)} - \frac{q - median(q)}{\sqrt{2}MAD(q)}$$

Eq. 7

409

410 with p and q being the residual series of the reference station and the neighbor station, respectively.
411 For each station there are $j - 1$ correlation coefficients r_{MAD}. In order to decide the cut-off distance
412 that a neighbor station will be considered in the analysis we plot r_{MAD} coefficient against its distance
413 from the reference station (Fig. 5). Based on results from all stations we decide to set a cut-off at 1500
414 km, slightly higher than the 1350 km suggested by Kreemer and Blewitt (2021). The 1500 km cut-off
415 allows us to separate stations between East and West coast, as spatially coherent signals at stations
416 located across the continent are negligible.
417 4) Derive the median slope estimator (ccs) using Theil-Sen median trend. ccs is the median trend of the
418 r_{MAD} coefficients of a station against their distance with the reference station.
419 5) Derive the zero-distance intercept cci_j for each station as median($r_{MAD} - ccs * d$), with d being the
420 distance between the station of reference and the neighbor station (maximum d = 1500 km).

421   6) Construct CMC: Calculate the cumulative (c_j) and percentile (p_j) weights for each station and then
422   find the weighted median that corresponds to $p_j = 50\%$. This weighted median represents the CMC of
423   the station (Fig. 6).
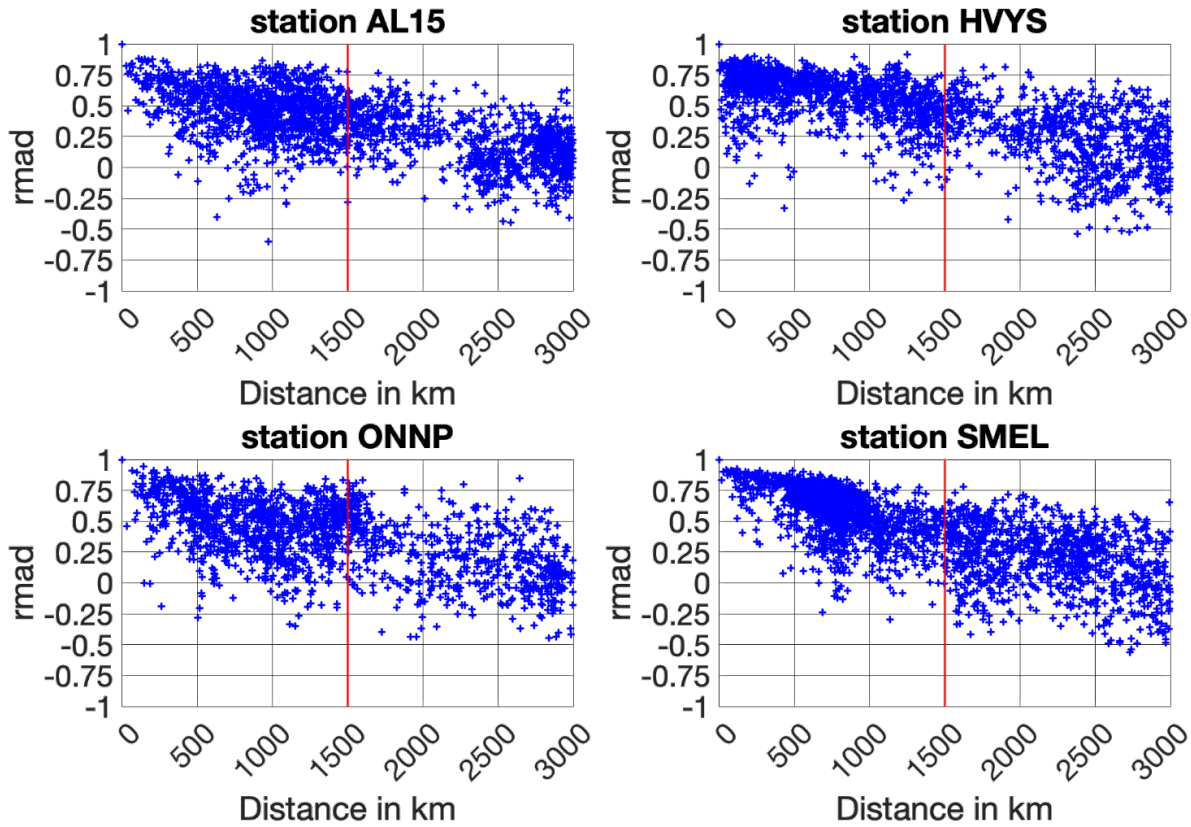
424
425   Figure 5: r_{MAD} coefficient of four random stations with the rest of the station sample, plotted against the
426   distance of the reference station with the rest of the stations. Each cross resembles the r_{MAD} of the
427   reference station with a station located at distance d.
428
429   CMC is limited in providing a realistic error approximation, in that the technique cannot isolate spatially
430   correlated noise from signal (e.g., hydrology signals not described by the trajectory model are present in
431   the residuals fed into CMC). Under the realistic assumption that a component of the high frequency signal
432   contained in CMC reflects real hydrological processes, we remove the contribution of surface hydrology
433   using Global Land Data Assimilation System (GLDAS) (Rodell et al., 2004) vertical displacement
434   estimates. GLDAS does not model deep groundwater and open surface water, so these signals remain in
435   the residual (Scanlon et al., 2018). Vertical displacement estimates driven by surface hydrology are
436   derived similar to GRACE(-FO) (Section 2.2). We use Noah v2.1 monthly estimates of soil moisture
437   storage given at 0.25-degree grids (Beaudoing and Rodell, 2016), convert the fields from terrestrial water
438   storage (kg/m^2) to units of equivalent water height, derive the spherical harmonic coefficients of the
439   equivalent water height mass load using Wahr et al. (1998), and predict the elastic response of the Earth
440   (Eq. 1). Afterwards, we remove the reference epoch (09/2012) similar to GPS and estimate the vertical
441   displacement at the locations of the GPS sites by interpolating the estimates of the closest neighbors to the
442   station's location. Note, that because our interest is to prepare the data for a combined solution with
443   GRACE(-FO) we interpolate the timeseries at the times of GRACE(-FO) monthly series availability. The

444 interested reader is referred to the supplement, where we show the vertical displacement estimated by
445 GPS, GRACE(-FO) and GLDAS (Figure S2) for randomly selected stations. Finally, we derive residuals
446 relative to the trajectory model (Eq. 2). GLDAS (surface hydrology) residuals should ideally reflect high
447 frequency hydrological processes and are therefore removed from GPS residuals. Overall, CMC of
448 surface hydrology residuals exhibits a fairly small magnitude (~0.5 mm). We remove the contribution of
449 surface hydrology within the CMC algorithm by first subtracting GLDAS vertical displacement estimates
450 from GPS, and next inputting the residuals of this difference into the algorithm. The output of this process
451 (CMC$_{HF}$) slightly decreases the magnitude of CMC and expresses a more realistic representation of
452 spatially correlated noise.
453
454 3.2 Results
455
456 Vertical displacement uncertainty of each station is estimated by means of all the different approaches
457 discussed in Section 3. Mean (μ), median and standard deviation (std) values are shown in Table 1. On
458 average, an assumption of white noise shows slightly reduced uncertainty compared to the other
459 techniques, followed by RMSE. When flicker noise is considered in addition to white noise (WN+FN) the
460 average uncertainty increases by nearly 0.8 mm compared to the white noise only. We note that the
461 contribution of white noise in the case of WN+FN is negligible for ninety seven percent of the stations
462 (that is flicker noise describes the noise exclusively). Noise level from combination of all three noise
463 models (WN+FN+RW) is less than 4 mm on average. In this case too, white noise is negligible, and noise
464 is described exclusively from flicker noise for 1550 stations, and from random walk for 600 stations. The
465 rest of the data sample reflects a contribution from both noise models. We additionally analyzed the
466 amplitude of the noise of each noise model (σ_{PL}) with respect to the length of the input series. Results did
467 not identify any clear relationship between σ_{PL} and the length of each station's timeseries. CMC noise
468 floor is 3.6 mm on average with a relatively large standard deviation (±1.6 mm) which suggests that
469 spatially correlated noise has higher variability than time-correlated noise (± 1.6 mm as opposed to ~±1
470 mm). When surface hydrology is removed (CMC$_{HF}$) the noise floor drops by a fraction of a mm on
471 average compared to CMC.
472
473 Table 1: Different uncertainty quantification cases

	mean (μ) (mm)	median (mm)	± std (mm)
RMSE	2.8	2.7	0.8
WN	2.4	2.2	0.8
WN+FN	3.2	3.1	0.7
WN+FN+RW	3.8	3.5	1.1
CMC	3.6	3.2	1.6
CMC$_{HF}$	3.5	3.1	1.6

474
475 RMSE and WN exhibit a smooth transition among the regions, which indicates the presence of spatially
476 coherent regime signal mostly driven by hydrology (Fig. 6). The combination of WN+FN is mostly
477 dominated by FN and the uncertainty exhibits local (in space) coherence. The uncertainty is larger when

478   random walk is included in the combination (WN+FN+RW). A recent study from Argus et al. (2022) on
479   groundwater flux in Central Valley (California) suggests that noise on GPS-derived uplift motion can be
480   well described by a combination of flicker noise and random walk, due to the ability of these noise
481   models to reflect low frequency noise. When a simulated contribution of the surface hydrological
482   component is removed from the series, CMC_{HF} reflects a more realistic picture of the noise. Arguably the
483   level of change compared to CMC is sub-millimeter. Signal contributions from un-modelled groundwater
484   variations are potentially still present, but groundwater changes are typically slower in time.
485
486
487   We obtain the relative likelihood of each uncertainty quantification method by estimating the probability
488   density function (PDF) (Fig. 7). White noise has a flat power spectrum, having the same amplitude
489   across frequencies. Estimating a best fit for a flat spectrum doesn't allow for capturing the long tail skew
490   of the residuals (low frequency), which are biased towards their mean. Thus, the amplitude of white noise
491   is smaller compared to the rest of the techniques (Table 1). Flicker and random walk noise models add to
492   the long tail of the power distribution, that is they allow more low frequency noise, which explains the
493   higher amplitude of the uncertainty when these two noise types are considered.
494   RMSE and WN show a 50% probability of a station having an uncertainty (σ) between 1.5-2 mm and less
495   than 10% of a station exceeding $\sigma=4$ mm. The noise level fells within [2 4] mm for ~93% of the stations
496   when we consider combination of WN+FN. PDF of RMSE, WN and WN+FN resemble a normal
497   distribution, with the mean being shifted for each case. When random walk is also considered
498   (WN+FN+RW) 64% of the stations exhibit noise within [2 4] mm. In this case, the distribution is more
499   spread resembling a gamma-like distribution, with a peak being at 3 mm (18%). CMC and CMC_{HF} PDF
500   also follow a gamma-shape, and the probability of the uncertainty ranging between [2 4] mm is nearly
501   60% for CMC and 65% when surface hydrology is removed.
502
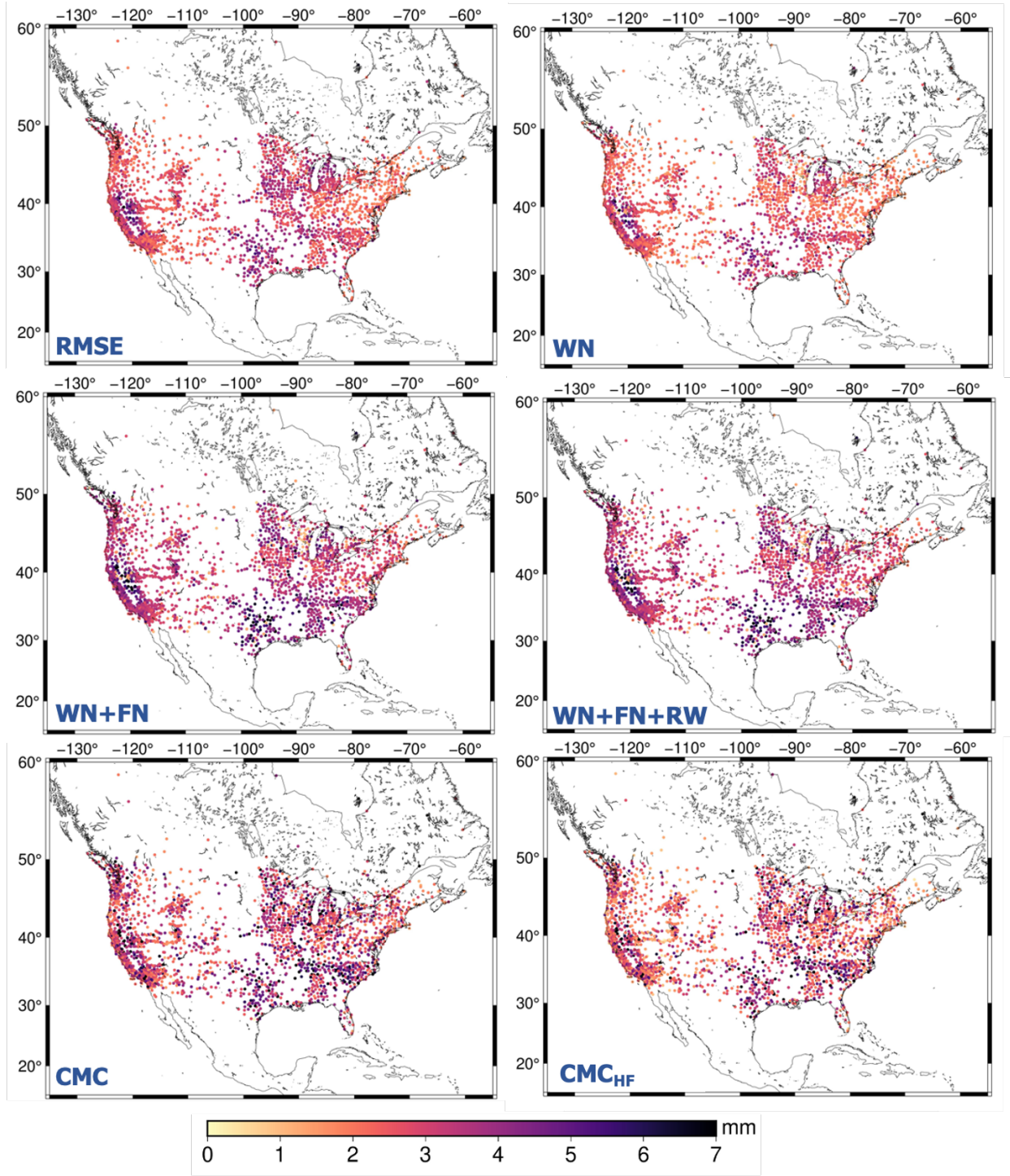
503
504   Figure 6: Noise amplitudes of GPS timeseries estimated using different techniques.
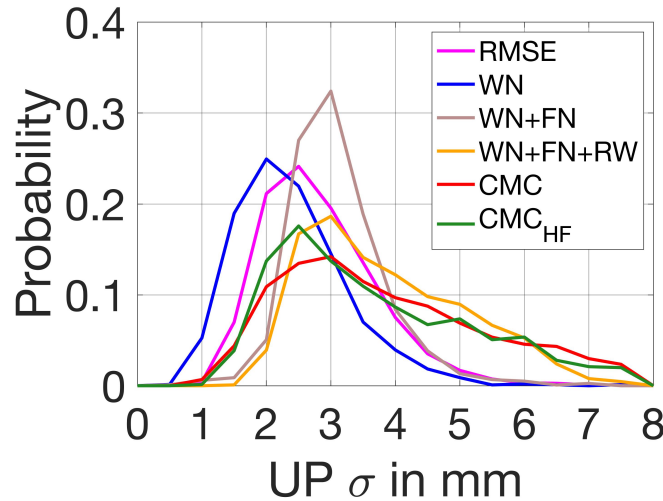
505

Figure 7: Probability density function of vertical displacement estimates uncertainty

4. Conclusions and Discussion

GPS-derived vertical displacements are very useful for supplementing GRACE(-FO) gravity products to infer mass change signals at spatial scales smaller than what can typically be achieved with current satellite gravimetry alone (i.e., < 300km). This work provides a general workflow to isolate elastic surface mass signals from GPS vertical displacement, by developing processing standards; additionally, it suggests uncertainty quantification schemes to quantify error on GPS vertical displacement estimates. The ultimate goal is to prepare GPS estimates for merging with satellite-gravimetry observations. First, we provide a list of corrections needed for isolating surface mass following recommendations outlined in Argus et al. (2017; 2022). Additionally, a detailed investigation of trends, correlation, and variance reduction highlights the need for better background modeling (glacial isostatic adjustment and interseismic strain), as the two observation techniques respond differently in the presence of such errors. At this point the recommendation is to remove sites located in the vicinity of regions where background models are known to perform poorly, before any joint inversion. Except detecting outlier stations, screening metrics point to extra corrections that need to be applied in certain sites (e.g., missed antenna offsets).

Several uncertainty quantification schemes have been tested to prescribe weights on GPS vertical displacement estimates that are needed for a joint inversion with GRACE(-FO) data. The average noise level indicated by RMSE is 2.8 mm. White noise average is 2.5 mm. The errors increase when lower frequencies are included in the noise estimation. When we account for flicker noise, one third of the sites exhibits noise levels of up to 3 mm. The average noise increases significantly in presence of random walk, as more power of the lower frequencies gets into the estimations, and the distribution of noise is more dispersed. In this case, half of the stations are prescribed with > 4 mm uncertainty. Argus et al. (2022), finds that random walk is the most realistic representation of noise based on postfit residuals. We notice that the spectrum of CMC provides similar uncertainties to random walk, which implies that despite the different characterization procedure, CMC is able to provide equally realistic noise estimates of GPS timeseries. We attempted to minimize lingering hydrology signals embedded in CMC, through

reducing the GPS vertical displacement observations with displacements from the GLDAS hydrology
model. The average noise floor dropped slightly (~0.5 mm drop in sigma). Future work will provide
further information of GPS station errors when the weight of each GPS site is also considered based on its
impact on the performance in a formal data combination of GPS-GRACE(-FO). The suggested
framework can be easily adjusted to account for global datasets. The new dataset provides GPS vertical
displacements of elastic mass variations in North America and their associated uncertainties.

References

Akaike, H.: A new look at the statistical model identification. IEEE transactions on automatic control,
19(6), pp.716-723. https://doi.org/10.1109/TAC.1974.1100705, 1974.

Altamimi, Z., Rebischung, P., Métivier, L. and Collilieux, X.: ITRF2014: A new release of the
International Terrestrial Reference Frame modeling nonlinear station motions. Journal of Geophysical
Research: Solid Earth, 121(8), pp.6109-6131. https://doi.org/10.1002/2016JB013098, 2016.

Amiri-Simkooei, A.R., Mohammadloo, T.H. and Argus, D.F: Multivariate analysis of GPS position
timeseries of JPL second reprocessing campaign. Journal of Geodesy, 91, pp.685-704.
https://doi.org/10.1007/s00190-016-0991-9, 2017.

Argus, D.F., Fu, Y. and Landerer, F.W.: Seasonal variation in total water storage in California inferred
from GPS observations of vertical land motion. Geophysical Research Letters, 41(6), pp.1971-1980.
https://doi.org/10.1002/2014GL059570, 2014.

Argus, D.F., Gordon, R.G., Heflin, M.B., Ma, C., Eanes, R.J., Willis, P., Peltier, W.R. and Owen, S.E.:
The angular velocities of the plates and the velocity of Earth's centre from space geodesy. Geophysical
Journal International, 180(3), pp.913-960. https://doi.org/10.1111/j.1365-246X.2009.04463.x, 2010.

Argus, D.F., Landerer, F.W., Wiese, D.N., Martens, H.R., Fu, Y., Famiglietti, J.S., Thomas, B.F., Farr,
T.G., Moore, A.W. and Watkins, M.M.: Sustained water loss in California's mountain ranges during
severe drought from 2012 to 2015 inferred from GPS. Journal of Geophysical Research: Solid Earth,
122(12), pp.10-559. https://doi.org/10.1002/2017JB014424, 2017.

580

581 Argus, D. F., Peltier, W. R., Drummond, R. and Moore, A. W: The Antarctica component of postglacial
582 rebound model ICE-6G_C (VM5a) based on GPS positioning, exposure age dating of ice thicknesses, and
583 relative sea level histories. Geophysical Journal International, 198, 537–563.
584 https://doi.org/10.1093/gji/ggu140, 2014.

585

586 Argus, D.F., Martens, H.R., Borsa, A.A., Knappe, E., Wiese, D.N., Alam, S., Anderson, M., Khatiwada,
587 A., Lau, N., Peidou, A. and Swarr, M.: Subsurface water flux in California's Central Valley and its source
588 watershed from space geodesy. Geophysical Research Letters, 49(22), p.e2022GL099583.
589 https://doi.org/10.1029/2022GL099583, 2022.

590

591 Argus, D.F., Peltier, W.R., Blewitt, G. and Kreemer, C.: The Viscosity of the Top Third of the Lower
592 Mantle Estimated Using GPS, GRACE, and Relative Sea Level Measurements of Glacial Isostatic
593 Adjustment. Journal of Geophysical Research: Solid Earth, 126(5), p.e2020JB021537.
594 https://doi.org/10.1029/2020JB021537, 2021.

595

596 Beaudoing, H. and M. Rodell: GLDAS Noah Land Surface Model L4 monthly 0.25 x 0.25 degree V2.1,
597 Greenbelt, Maryland, USA, Goddard Earth Sciences Data and Information Services Center (GES DISC).
598 https://doi.org/10.5067/SXAVCZFAQLNO, 2020.

599

600 Becker, J.M. and Bevis, M.: Love's problem. Geophysical Journal International, 156(2), pp.171-178.
601 https://doi.org/10.1111/j.1365-246X.2003.02150.x, 2004.

602

603 Bertiger, W., Bar-Sever, Y., Dorsey, A., Haines, B., Harvey, N., Hemberger, D., Heflin, M., Lu, W.,
604 Miller, M., Moore, A.W. and Murphy, D.: GipsyX/RTGx, a new tool set for space geodetic operations
605 and research. Advances in space research, 66(3), pp.469-489. https://doi.org/10.1016/j.asr.2020.04.015,
606 2020.

607

608 Bevis, M. and Brown, A.: Trajectory models and reference frames for crustal motion geodesy (2014).
609 Journal of Geodesy, 88, 283–311, doi: 10.1007/s00190-013-0685-5.

610

611 Blewitt, G., Hammond, W.C. and Kreemer, C.: Harnessing the GPS data explosion for interdisciplinary
612 science. Eos, 99(10.1029), p.485. doi.org/10.1029/2018EO104623.
613 https://doi.org/10.1029/2018EO104623, 2018.

614

615 Blewitt, G., Lavallée, D., Clarke, P. and Nurutdinov, K.: A new global mode of Earth deformation:
616 Seasonal cycle detected. Science, 294(5550), pp.2342-2345.
617 https://doi.org/10.1126/science.1065328, 2001.

618

619 Boehm, J., Werl, B., and Schuh, H.: Troposphere mapping functions for GPS and very long baseline
620 interferometry from European Centre for Medium-Range Weather Forecasts operational analysis data, *J.*
621 *Geophys. Res.*, 111, B02406, doi:10.1029/2005JB003629, 2006.

622

623   Borsa, A.A., Agnew, D.C. and Cayan, D.R.: December. Drought-induced uplift in the western United
624   States as observed by the EarthScope Plate Boundary Observatory GPS network. In AGU Fall Meeting
625   Abstracts (Vol. 2014, pp. G23B-0481), 2014.
626
627   Bos, M.S., Fernandes, R.M.S., Williams, S.D.P. and Bastos, L.: Fast error analysis of continuous GPS
628   observations. Journal of Geodesy, 82(3), pp.157-166. https://doi.org/10.1007/s00190-007-0165-x, 2008.
629
630   Bos, M.S., Fernandes, R.M.S., Williams, S.D.P. and Bastos, L.: Fast error analysis of continuous GPS
631   observations with missing data. Journal of Geodesy, 87(4), pp.351-360. https://doi.org/10.1007/s00190-
632   012-0605-0, 2013.
633
634   Chew, C.C. and Small, E.E.: Terrestrial water storage response to the 2012 drought estimated from GPS
635   vertical position anomalies. Geophysical Research Letters, 41(17), pp.6145-6151.
636   https://doi.org/10.1002/2014GL061206, 2014.
637
638   Crowell, B.W., Bock, Y. and Liu, Z.: Single-station automated detection of transient deformation in GPS
639   timeseries with the relative strength index: A case study of Cascadian slow slip. Journal of Geophysical
640   Research: Solid Earth, 121(12), pp.9077-9094. https://doi.org/10.1002/2016JB013542, 2016.
641
642   Davis, J.L., Elósegui, P., Mitrovica, J.X. and Tamisiea, M.E.: Climate-driven deformation of the solid
643   Earth from GRACE and GPS. Geophysical Research Letters, 31(24).
644   https://doi.org/10.1029/2004GL021435, 2004.
645
646   Dee, D.P., Uppala, S.M., Simmons, A.J., Berrisford, P., Poli, P., Kobayashi, S., Andrae, U., Balmaseda,
647   M.A., Balsamo, G., Bauer, D.P. and Bechtold, P.: The ERA-Interim reanalysis: Configuration and
648   performance of the data assimilation system. Quarterly Journal of the royal meteorological society,
649   137(656), pp.553-597. https://doi.org/10.1002/qj.828, 2011.
650
651   Dill, R., and Dobslaw, H.: Numerical simulations of global-scale high resolution hydrological crustal
652   deformations. Journal of Geophysical Research: Solid Earth, 118(9), 5008–5017.
653   https://doi.org/10.1002/jgrb.50353, 2013.
654
655   Dobslaw, H., Bergmann-Wolf, I., Dill, R., Poropat, L., Thomas, M., Dahle, C., Esselborn, S., König, R.
656   and Flechtner, F.: A new high-resolution model of non-tidal atmosphere and ocean mass variability for
657   de-aliasing of satellite gravity observations: AOD1B RL06. Geophysical Journal International, 211(1),
658   pp.263-269. https://doi.org/10.1093/gji/ggx302, 2017.
659
660   Dong, D., Fang, P., Bock, Y., Webb, F., Prawirodirdjo, L., Kedar, S., and Jamason, P.: Spatiotemporal
661   filtering using principal component analysis and Karhunen-Loeve expansion approaches for regional GPS
662   network analysis, *J. Geophys. Res.*, 111, B03405, https://doi.org/10.1029/2005JB003806, 2006.
663
664   Frederikse, T., Landerer, F., Caron, L., Adhikari, S., Parkes, D., Humphrey, V.W., Dangendorf, S.,
665   Hogarth, P., Zanna, L., Cheng, L. and Wu, Y.H.: The causes of sea-level rise since 1900. Nature,
666   584(7821), pp.393-397. https://doi.org/10.1038/s41586-020-2591-3, 2020.

667

668 Fu, Y. and Freymueller, J.T.: Seasonal and long-term vertical deformation in the Nepal Himalaya
669 constrained by GPS and GRACE measurements. Journal of Geophysical Research: Solid Earth, 117(B3).
670 https://doi.org/10.1029/2011JB008925, 2012.

671

672 Fu, Y., Argus, D.F. and Landerer, F.W.: GPS as an independent measurement to estimate terrestrial water
673 storage variations in Washington and Oregon. Journal of Geophysical Research: Solid Earth, 120(1),
674 pp.552-566. https://doi.org/10.1002/2014JB011415, 2015.

675

676 Fukumori, I., Wang, O., Llovel, W., Fenty, I. and Forget, G.: A near-uniform fluctuation of ocean bottom
677 pressure and sea level across the deep ocean basins of the Arctic Ocean and the Nordic Seas. Progress in
678 Oceanography, 134, pp.152-172. https://doi.org/10.1016/j.pocean.2015.01.013, 2015.

679

680 Gazeaux, J., Williams, S., King, M., Bos, M., Dach, R., Deo, M., Moore, A.W., Ostini, L., Petrie, E.,
681 Roggero, M. and Teferle, F.N.: Detecting offsets in GPS timeseries: First results from the detection of
682 offsets in GPS experiment. Journal of Geophysical Research: Solid Earth, 118(5), pp.2397-2407.
683 https://doi.org/10.1002/jgrb.50152, 2013.

684

685 Haines, B., Bar-Sever, Y., Bertiger, W., Desai, S. and Willis, P. One-centimeter orbit determination for
686 Jason-1: new GPS-based strategies. *Marine Geodesy*, *27*(1-2), pp.299-318.
687 https://doi.org/10.1007/BF03321179, 2004.

688

689 Hammond, W. C., Blewitt, G., and Kreemer, C.: GPS Imaging of vertical land motion in California and
690 Nevada: Implications for Sierra Nevada uplift, *J. Geophys. Res. Solid Earth*, 121, 7681–7703,
691 doi:10.1002/2016JB013458, 2016.

692

693 He, X., Bos, M.S., Montillet, J.P. and Fernandes, R.M.S.: Investigation of the noise properties at low
694 frequencies in long GPS timeseries. Journal of Geodesy, 93(9), pp.1271-1282.
695 https://doi.org/10.1007/s00190-019-01244-y, 2019.

696

697 Houborg, R., Rodell, M., Li, B., Reichle, R. and Zaitchik, B.F.: Drought indicators based on model-
698 assimilated Gravity Recovery and Climate Experiment (GRACE) terrestrial water storage observations.
699 Water Resources Research, 48(7). https://doi.org/10.1029/2011WR011291, 2012.

700

701 Ji, K.H. and Herring, T.A. A method for detecting transient signals in GPS position timeseries: smoothing
702 and principal component analysis. Geophysical Journal International, 193(1), pp.171-186.
703 https://doi.org/10.1093/gji/ggt003, 2013.

704

705 Jiang, W., Li, Z., van Dam, T. and Ding, W.: Comparative analysis of different environmental loading
706 methods and their impacts on the GPS height timeseries. Journal of Geodesy, 87(7), pp.687-703.
707 https://doi.org/10.1007/s00190-013-0642-3, 2013.

708

709   Klos, A., Bogusz, J., Figurski, M. and Kosek, W.: Uncertainties of geodetic velocities from permanent
710   GPS observations: the Sudeten case study. Acta Geodynamica et Geomaterialia, 11(3), p.175.
711   https://doi.org/10.13168/AGG.2014.0005, 2014.

712

713   Klos, A., Dobslaw, H., Dill, R. and Bogusz, J.: Identifying the sensitivity of GPS to non-tidal loadings at
714   various time resolutions: examining vertical displacements from continental Eurasia. GPS Solutions,
715   25(3), p.89. https://doi.org/10.1007/s10291-021-01135-w, 2021.

716

717   Klos, A., Kusche, J., Fenoglio-Marc, L., Bos, M.S. and Bogusz, J.: Introducing a vertical land
718   displacement model for improving estimates of sea level rates derived from tide gauge records affected by
719   earthquakes. GPS Solutions, 23(4), pp.1-12. https://doi.org/10.1007/s10291-019-0896-1, 2019.

720

721   Klos, A., Kusche, J., Leszczuk, G., Gerdener, H., Schulze, K., Lenczuk, A. and Bogusz, J.: Introducing
722   the Idea of Classifying Sets of Permanent GNSS Stations as Benchmarks for Hydrogeodesy. *Journal of*
723   *Geophysical Research: Solid Earth*, *128*(9), p.e2023JB026988. https://doi.org/10.1029/2023JB026988,
724   2023.

725

726   Kreemer, C. and Blewitt, G.: Robust estimation of spatially varying common-mode components in GPS
727   timeseries. Journal of geodesy, 95(1), pp.1-19. https://doi.org/10.1007/s00190-020-01466-5, 2021.

728

729   Kumar, U., Chao, B.F. and Chang, E.T.: What causes the common-mode error in array GPS displacement
730   fields: Case study for Taiwan in relation to atmospheric mass loading. Earth and Space Science, 7(11),
731   p.e2020EA001159. https://doi.org/10.1029/2020EA001159, 2020.

732

733   Landerer, F.W., Flechtner, F.M., Save, H., Webb, F.H., Bandikova, T., Bertiger, W.I., Bettadpur, S.V.,
734   Byun, S.H., Dahle, C., Dobslaw, H. and Fahnestock, E.: Extending the global mass change data record:
735   GRACE Follow-On instrument and science data performance. Geophysical Research Letters, 47(12),
736   p.e2020GL088306. https://doi.org/10.1029/2020GL088306, 2020.

737

738   Li, S., Wang, K., Wang, Y., Jiang, Y. and Dosso, S.E.: Geodetically inferred locking state of the Cascadia
739   megathrust based on a viscoelastic Earth model. Journal of Geophysical Research: Solid Earth, 123(9),
740   pp.8056-8072. https://doi.org/10.1029/2018JB015620, 2018.

741

742   Li, W. and Shen, Y.: The consideration of formal errors in spatiotemporal filtering using principal
743   component analysis for regional GPS position timeseries. Remote Sensing, 10(4), p.534.
744   https://doi.org/10.3390/rs10040534, 2018.

745

746   Liu, B., Dai, W., Peng, W. and Meng, X.: Spatiotemporal analysis of GPS timeseries in vertical direction
747   using independent component analysis. Earth, Planets and Space, 67(1), pp.1-10.
748   https://doi.org/10.1186/s40623-015-0357-1, 2015.

749

750   Loomis, B.D., Rachlin, K.E. and Luthcke, S.B.: Improved Earth oblateness rate reveals increased ice
751   sheet losses and mass-driven sea level rise. Geophysical Research Letters, 46(12), pp.6910-6917.
752   https://doi.org/10.1029/2019GL082929, 2019.

753

Martens, H. R., Argus, D. F., Norberg, C., Blewitt, G., Herring, T. A., Moore, A. W., et al.: Atmospheric pressure loading in GPS positions: Dependency on GPS processing methods and effect on assessment of seasonal deformation in the contiguous USA and Alaska. Journal of Geodynamics, 94(12), 115, https://doi.org/10.1007/s00190-020-01445-w, 2020.

Michel, A., Santamaría-Gómez, A., Boy, J.P., Perosanz, F. and Loyer, S.: Analysis of GPS Displacements in Europe and Their Comparison with Hydrological Loading Models. Remote Sensing, 13(22), p.4523. https://doi.org/10.3390/rs13224523, 2021.

Milliner, C., Materna, K., Bürgmann, R., Fu, Y., Moore, A.W., Bekaert, D., Adhikari, S. and Argus, D.F.: Tracking the weight of Hurricane Harvey's stormwater using GPS data. Science advances, 4(9), p.eaau2477. https://doi.org/10.1126/sciadv.aau2477, 2018.

Montillet, J.P., Melbourne, T.I. and Szeliga, W.M.: GPS vertical land displacement corrections to sea-level rise estimates in the Pacific Northwest. Journal of Geophysical Research: Oceans, 123(2), pp.1196-1212. https://doi.org/10.1002/2017JC013257, 2018.

NASA Jet Propulsion Laboratory (JPL): GRACE-FO Monthly Geopotential Spherical Harmonics JPL Release 6.0, https://doi.org/10.5067/GFL20-MJ060, 2019.

Nikolaidis, R.: Observation of geodetic and seismic deformation with the Global Positioning System. University of California, San Diego, 2002.

Pail, R., Bingham, R., Braitenberg, C., Dobslaw, H., Eicker, A., Güntner, A., Horwath, M., Ivins, E., Longuevergne, L., Panet, I. and Wouters, B.: Science and user needs for observing global mass transport to understand global change and to benefit society. Surveys in Geophysics, 36(6), pp.743-772. https://doi.org/10.1007/s10712-015-9348-9, 2015.

Peltier, W. R., Argus, D. F. and Drummond, R. :Space geodesy constrains ice age terminal deglaciation: The global ICE-6G_C (VM5a) model. Journal Geophysical Research: Solid Earth, 120, 450–487. https://doi.org/10.1002/2014JB011176, 2015.

Peltier, W. R., Argus, D. F., and Drummond, R.: Comment on the paper by Purcell et al. 2016 entitled 'An assessment of ICE-6G_C (VM5a) glacial isostatic adjustment model (2018). Journal Geophysical Research: Solid Earth, 122, 2019-2028. https://doi.org/10.1002/2016JB013844, 2018.

Luzum, B. and Petit, G. (2012). The IERS Conventions: Reference systems and new models. *Proceedings of the International Astronomical Union, 10*(H16), 227-228. https://doi:10.1017/S1743921314005535, 2012.

Ray, J., Altamimi, Z., Collilieux, X. and van Dam, T.: Anomalous harmonics in the spectra of GPS position estimates. GPS solutions, 12, pp.55-64. https://doi.org/10.1007/s10291-007-0067-7, 2008.

797 Reager, J.T., Thomas, B.F. and Famiglietti, J.S.: River basin flood potential inferred using GRACE
798 gravity observations at several months lead time. Nature Geoscience, 7(8), pp.588-592.
799 https://doi.org/10.1038/ngeo2203, 2014.
800
801 Rodell, M., Houser, P.R., Jambor, U.E.A., Gottschalck, J., Mitchell, K., Meng, C.J., Arsenault, K.,
802 Cosgrove, B., Radakovich, J., Bosilovich, M. and Entin, J.K.: The global land data assimilation system.
803 Bulletin of the American Meteorological society, 85(3), pp.381-394.
804 https://doi.org/10.1175/BAMS-85-3-381, 2004.
805
806 Rodriguez-Solano, C.J., Hugentobler, U., Steigenberger, P., Bloßfeld, M. and Fritsche, M.: Reducing the
807 draconitic errors in GPS geodetic products. Journal of Geodesy, 88(6), pp.559-574.
808 https://doi.org/10.1007/s00190-014-0704-1, 2014.
809
810 Rui, H., Beaudoing, H. and Loeser, C.: README document for NASA GLDAS version 2 data products.
811 Goddart Earth Sciences Data and Information Services Center (GES DISC): Greenbelt, MD, USA, 2018.
812
813 Santamaria-Gomez, A., Gravelle, M., Collilieux, X., Guichard, M., Míguez, B.M., Tiphaneau, P. and
814 Wöppelmann, G.: Mitigating the effects of vertical land displacement in tide gauge records using a state-
815 of-the-art GPS velocity field. Global and Planetary Change, 98, pp.6-17.
816 https://doi.org/10.1016/j.gloplacha.2012.07.007, 2012.
817
818 Schwarz, G.: Estimating the dimension of a model. Annals of statistics, 6(2), pp.461-464.
819 https://doi.org/10.1214/aos/1176344136, 1978.
820
821 Serpelloni, E., Faccenna, C., Spada, G., Dong, D. and Williams, S.D.: Vertical GPS ground motion rates
822 in the Euro-Mediterranean region: New evidence of velocity gradients at different spatial scales along the
823 Nubia-Eurasia plate boundary. Journal of Geophysical Research: Solid Earth, 118(11), pp.6003-6024.
824 https://doi.org/10.1002/2013JB010102, 2013.
825
826 Simmons, A., Uppala, S., Dee, D. and Kobayashi, S.: ERA-Interim: New ECMWF reanalysis products
827 from 1989 onwards. ECMWF newsletter, 110, 25-35. https://doi.org/10.21957/pocnex23c6, 2007.
828
829 Sun, Y., Riva, R. and Ditmar, P.: Optimizing estimates of annual variations and trends in geocenter
830 motion and J2 from a combination of GRACE data and geophysical models, J. Geophys. Res. Solid Earth,
831 121, https://doi:10.1002/2016JB013073, 2016.
832
833 Tapley, B.D., Watkins, M.M., Flechtner, F., Reigber, C., Bettadpur, S., Rodell, M., Sasgen, I.,
834 Famiglietti, J.S., Landerer, F.W., Chambers, D.P. and Reager, J.T.: Contributions of GRACE to
835 understanding climate change. Nature climate change, 9(5), pp.358-369.
836 https://doi.org/10.1038/s41558-019-0456-2, 2019.
837
838 Thomas, A.C., Reager, J.T., Famiglietti, J.S. and Rodell, M.: A GRACE-based water storage deficit
839 approach for hydrological drought characterization. Geophysical Research Letters, 41(5), pp.1537-1545.
840 https://doi.org/10.1002/2014GL059323, 2014.

841

842 Thomas, B.F., Famiglietti, J.S., Landerer, F.W., Wiese, D.N., Molotch, N.P. and Argus, D.F.:
843 Groundwater drought index: Evaluation of California Central Valley groundwater drought. Remote
844 Sensing of Environment, 198, pp.384-392. https://doi.org/10.1016/j.rse.2017.06.026, 2017.

845

846 Tian, Y. and Shen, Z.K.: Extracting the regional common-mode component of GPS station position
847 timeseries from dense continuous network. Journal of Geophysical Research: Solid Earth, 121(2),
848 pp.1080-1096. https://doi.org/10.1002/2015JB012253, 2016.

849

850 Tregoning, P., Watson, C., Ramillien, G., McQueen, H. and Zhang, J.: Detecting hydrologic deformation
851 using GRACE and GPS. Geophysical Research Letters, 36(15). https://doi.org/10.1029/2009GL038718,
852 2009.

853

854 Tsai, V.C.: A model for seasonal changes in GPS positions and seismic wave speeds due to thermoelastic
855 and hydrologic variations. Journal of Geophysical Research: Solid Earth, 116(B4).
856 https://doi.org/10.1029/2010JB008156, 2011.

857

858 van Dam, T., Wahr, J. and Lavallée, D.: A comparison of annual vertical crustal displacements from GPS
859 and Gravity Recovery and Climate Experiment (GRACE) over Europe. Journal of Geophysical Research:
860 Solid Earth, 112(B3). https://doi.org/10.1029/2006JB004335, 2007.

861

862 Van Dam, T., Wahr, J., Milly, P.C.D., Shmakin, A.B., Blewitt, G., Lavallée, D. and Larson, K.M.: Crustal
863 displacements due to continental water loading. Geophysical Research Letters, 28(4), pp.651-654.
864 https://doi.org/10.1029/2000GL012120, 2001.

865

866 Velicogna, I., Mohajerani, Y., Landerer, F., Mouginot, J., Noel, B., Rignot, E., Sutterley, T., van den
867 Broeke, M., van Wessem, M. and Wiese, D.: Continuity of ice sheet mass loss in Greenland and
868 Antarctica from the GRACE and GRACE Follow-On missions. Geophysical Research Letters, 47(8),
869 p.e2020GL087291. https://doi.org/10.1029/2020GL087291, 2020.

870

871 Wahr, J., Molenaar, M. and Bryan, F.: Time variability of the Earth's gravity field: Hydrological
872 and oceanic effects and their possible detection using GRACE. *Journal of Geophysical*
873 *Research: Solid Earth*, *103*(B12), pp.30205-30229. https://doi.org/10.1029/98JB02844, 1998.

874

875 Wang, H., Xiang, L., Jia, L., Jiang, L., Wang, Z., Hu, B. and Gao, P.: Load Love numbers and Green's
876 functions for elastic Earth models PREM, iasp91, ak135, and modified models with refined crustal
877 structure from Crust 2.0. Computers & Geosciences, 49, pp.190-199.
878 https://doi.org/10.1016/j.cageo.2012.06.022, 2012.

879

880 Watkins, M.M., Wiese, D.N., Yuan, D.N., Boening, C. and Landerer, F.W.: Improved methods for
881 observing Earth's time variable mass distribution with GRACE using spherical cap mascons. Journal of
882 Geophysical Research: Solid Earth, 120(4), pp.2648-2671. https://doi.org/10.1002/2014JB011547, 2015.

883

884 Wdowinski, S., Bock, Y., Zhang, J., Fang, P. and Genrich, J.: Southern California permanent GPS
885 geodetic array: Spatial filtering of daily positions for estimating coseismic and postseismic displacements
886 induced by the 1992 Landers earthquake. Journal of Geophysical Research: Solid Earth, 102(B8),
887 pp.18057-18070. https://doi.org/10.1029/97JB01378, 1997.
888
889 Wessel, P., Luis, J.F., Uieda, L., Scharroo, R., Wobbe, F., Smith, W.H. and Tian, D.: The generic
890 mapping tools version 6. Geochemistry, Geophysics, Geosystems, 20(11), pp.5556-5564.
891 https://doi.org/10.1029/2019GC008515, 2019.
892
893 Wiese, D.N., Bienstock, B., Blackwood, C., Chrone, J., Loomis, B.D., Sauber, J., Rodell, M., Baize, R.,
894 Bearden, D., Case, K. and Horner, S.: The mass change designated observable study: overview and
895 results. Earth and Space Science, 9(8), p.e2022EA002311. https://doi.org/10.1029/2022EA002311, 2022.
896
897 Wiese, D.N., Landerer, F.W. and Watkins, M.M.: Quantifying and reducing leakage errors in the JPL
898 RL05M GRACE mascon solution. Water Resources Research, 52(9), pp.7490-7502.
899 https://doi.org/10.1002/2016WR019344, 2016.
900
901 Williams, S.D.: CATS: GPS coordinate timeseries analysis software. GPS solutions, 12(2), pp.147-153.
902 https://doi.org/10.1007/s10291-007-0086-4, 2008.
903
904 Williams, S.D., Bock, Y., Fang, P., Jamason, P., Nikolaidis, R.M., Prawirodirdjo, L., Miller, M. and
905 Johnson, D.J.: Error analysis of continuous GPS position timeseries. Journal of Geophysical Research:
906 Solid Earth, 109(B3). https://doi.org/10.1029/2003JB002741, 2004.
907
908 Wu, S., Nie, G., Liu, J., Wang, K., Xue, C., Wang, J., Li, H., Peng, F. and Ren, X.: A sub-regional
909 extraction method of common mode components from IGS and CMONOC stations in China. Remote
910 Sensing, 11(11), p.1389. https://doi.org/10.3390/rs11111389, 2019.
911
912 Yin, G., Forman, B.A., Loomis, B.D. and Luthcke, S.B.: Comparison of Vertical Surface Deformation
913 Estimates Derived From Space-Based Gravimetry, Ground-Based GPS, and Model-Based Hydrologic
914 Loading Over Snow-Dominated Watersheds in the United States. Journal of Geophysical Research: Solid
915 Earth, 125(8), p.e2020JB01943. https://doi.org/10.1029/2020JB019432, 2020.